Flexible Intelligent Metasurfaces for Enhanced MIMO Communications

Jiancheng An*, Chau Yuen*, Mérouane Debbah†, and Lajos Hanzo‡
*School of Electrical and Electronics Engineering, Nanyang Technological University, Singapore 639798
†Center for 6G, Khalifa University of Science and Technology, P O Box 127788, Abu Dhabi, UAE
‡School of Electronics and Computer Science, University of Southampton, SO17 1BJ Southampton, U.K.
E-mail: {jiancheng.an, chau.yuen}@ntu.edu.sg, merouane.debbah@ku.ac.ae, lh@ecs.soton.ac.uk

***Abstract*—Flexible intelligent metasurfaces (FIMs) constitute a promising technology that could significantly boost the wireless network capacity. An FIM is essentially a soft array made up of many low-cost radiating elements that can independently emit electromagnetic signals. What's more, each element can flexibly adjust its position, even perpendicularly to the surface, to morph the overall 3D shape. In this paper, we study the potential of FIMs in point-to-point multiple-input multiple-output (MIMO) communications, where two FIMs are used as transceivers. In order to characterize the capacity limits of FIM-aided narrowband MIMO transmissions, we formulate an optimization problem for maximizing the MIMO channel capacity by jointly optimizing the 3D surface shapes of the transmitting and receiving FIMs, as well as the transmit covariance matrix, subject to a specific total transmit power constraint and to the maximum morphing range of the FIM. To solve this problem, we develop an efficient block coordinate descent (BCD) algorithm. The BCD algorithm iteratively updates the 3D surface shapes of the FIMs and the transmit covariance matrix, while keeping the other fixed. Numerical results verify that FIMs can achieve higher MIMO capacity than traditional rigid arrays. In some cases, the MIMO channel capacity can be doubled by employing FIMs.**

***Index Terms*—Flexible intelligent metasurfaces (FIMs), multiple-input multiple-output (MIMO), reconfigurable intelligent surfaces (RIS).**

I. Introduction

Multiple-input multiple-output (MIMO) technologies aim to increase the data transmission rates by utilizing multiple antennas at both the source and destination. By tapping into channel state information (CSI) available at the transceivers and applying appropriate transmit precoding/receiver combining techniques, increased data rates can be achieved [1], [2]. In the fifth-generation (5G) networks, base stations (BSs) typically use large-scale antenna arrays having over 100 antennas [3]. Looking ahead, next-generation communication systems are expected to feature extremely large-scale antenna arrays with thousands of antennas for further enhancing data transmission capabilities [4], [5].

In practical MIMO communication systems, a significant challenge, particularly for mobile terminals, is fitting a large number of antenna elements into a limited physical area. A promising solution that is gaining traction is metasurface technology [6]. A metasurface is an artificially engineered planar structure made up of many sub-wavelength metallic or dielectric scattering particles [6], each of which is capable of independently radiating or scattering electromagnetic waves as desired [7]. Incorporating near-passive metasurfaces into wireless networks has great potential for 'reshaping' the wireless propagation environments [8]. Moreover, metasurfaces can also be used as reconfigurable antenna arrays due to their tunability and programmability [9], [10]. The dense arrays of metasurfaces enable electromagnetic operations at an unprecedented level of precision [11], which has led to the concept of holographic MIMO communications [12]–[15].

However, the existing MIMO technologies rely on rigid antenna arrays (RAAs) or metasurfaces having fixed element positions. As a further development, programmable flexible intelligent metasurfaces (FIM) have been developed [16]. This dynamic FIM is composed of a matrix of tiny metallic filaments, driven by reprogrammable Lorentz forces from electrical currents passing through a static magnetic field[1]. As a result, the FIM can promptly and precisely morph its surface shape. [16]. By strategically adjusting the physical position of each antenna element, multiple signal copies impinging from different paths may add constructively at the antenna array, thus effectively increasing the received signal power [17].

Motivated by this observation, we explore using FIMs as transceivers in a point-to-point MIMO communication system. Specifically, we focus our attention on maximizing the MIMO channel capacity by jointly optimizing the transmit signal covariance matrix and the 3D surface shapes of the transmitting and receiving FIMs, subject to realistic constraints on the total transmit power at the source and the maximum morphing range of the FIMs. Furthermore, we propose an efficient block coordinate descent (BCD) algorithm for iteratively optimizing the transmit covariance matrix and the 3D surface shapes of the FIMs. In each iteration, the optimal transmit covariance matrix is derived in a closed form based on the FIM's 3D surface shapes in the previous iteration, while the surface shapes of the FIMs are updated for the sake of increasing the channel capacity by utilizing a customized gradient ascent (GA) algorithm. Extensive numerical results validate the superior performance of the BCD algorithm compared to other benchmark schemes. The results indicate that by judiciously morphing the 3D surface shapes of the transmitting and receiving FIMs, the MIMO capacity is doubled in certain setups.

II. System Model

As illustrated in Fig. 1, we examine a point-to-point MIMO communication system where a pair of FIMs communicate with each other. One FIM is positioned at the source, while another is placed at the destination. The antenna arrays on the two FIMs are modeled as a flexible uniform planar array

[1]Please refer to https://www.eurekalert.org/multimedia/950133 for a video demonstrating the real-time surface-shape morphing capability of an FIM [16].

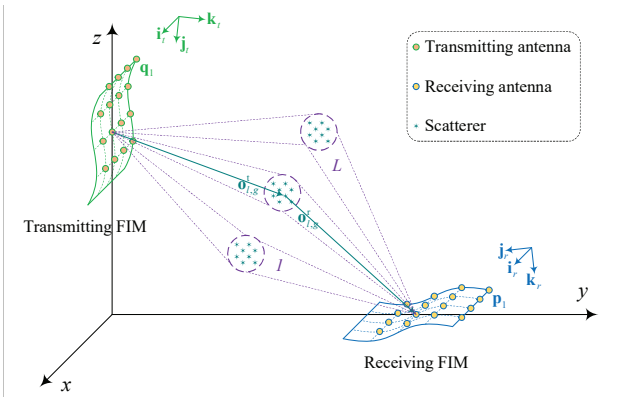

Fig. 1. Schematic of a point-to-point MIMO system, where an FIM is deployed at the source and another one is at the destination.

(UPA). In contrast to conventional MIMO systems, the position of each radiating element on the FIMs can be dynamically adjusted along the direction perpendicular to the surface, with the aid of a controller [16].

Specifically, let $\mathbf{i}_{\mathrm{t}} \in \mathbb{R}^3$ and $\mathbf{j}_{\mathrm{t}} \in \mathbb{R}^3$ represent the directions of the two sides of the transmitting FIM, while $\mathbf{k}_{\mathrm{t}} \in \mathbb{R}^3$ represents the normal direction of the transmitting FIM. Furthermore, let $\varphi_{\mathrm{t}} \in [0, \pi)$ and $\vartheta_{\mathrm{t}} \in [0, \pi)$ denote the azimuth and elevation angles, respectively, of the normal direction. Hence, $\mathbf{k}_{\mathrm{t}}$ can be expressed as $\mathbf{k}_{\mathrm{t}} = [\sin\vartheta_{\mathrm{t}}\cos\varphi_{\mathrm{t}}, \sin\vartheta_{\mathrm{t}}\sin\varphi_{\mathrm{t}}, \cos\vartheta_{\mathrm{t}}]^T$. Since $\mathbf{i}_{\mathrm{t}}$, $\mathbf{j}_{\mathrm{t}}$, and $\mathbf{k}_{\mathrm{t}}$ are orthogonal to each other, $\mathbf{i}_{\mathrm{t}}$ and $\mathbf{j}_{\mathrm{t}}$ can be readily derived, but the specific expressions are omitted, given the page limit. Similarly, let $\mathbf{i}_{\mathrm{r}} \in \mathbb{R}^3$ and $\mathbf{j}_{\mathrm{r}} \in \mathbb{R}^3$ represent the directions of the two sides of the receiving FIM, with $\mathbf{k}_{\mathrm{r}} \in \mathbb{R}^3$ representing its normal direction. Additionally, let $\varphi_{\mathrm{r}} \in [0, \pi)$ and $\vartheta_{\mathrm{r}} \in [0, \pi)$ represent the azimuth and elevation angles, respectively, of the normal direction of the receiving FIM. Therefore, the normal vector $\mathbf{k}_{\mathrm{r}}$ is expressed as $\mathbf{k}_{\mathrm{r}} = [\sin\vartheta_{\mathrm{r}}\cos\varphi_{\mathrm{r}}, \sin\vartheta_{\mathrm{r}}\sin\varphi_{\mathrm{r}}, \cos\vartheta_{\mathrm{r}}]^T$. Given that $\mathbf{i}_{\mathrm{r}}$, $\mathbf{j}_{\mathrm{r}}$, and $\mathbf{k}_{\mathrm{r}}$ are orthogonal to each other, $\mathbf{i}_{\mathrm{r}}$ and $\mathbf{j}_{\mathrm{r}}$ can be also derived.

Let $M = M_{\mathrm{x}}M_{\mathrm{y}}$ represent the number of transmitting antennas, with M_{x} and M_{y} denoting the number of antenna elements along the $\mathbf{i}_{\mathrm{t}}$ and $\mathbf{j}_{\mathrm{t}}$ directions, respectively. Let $\mathbf{q}_m \in \mathbb{R}^3,\ m = 1, \ldots, M$ represent the position of the m-th transmitting element. Similarly, let $N = N_{\mathrm{x}}N_{\mathrm{y}}$ represent the number of receiving antennas, with N_{x} and N_{y} denoting the number of antenna elements along the $\mathbf{i}_{\mathrm{r}}$ and $\mathbf{j}_{\mathrm{r}}$ directions, respectively. Let us furthermore denote the position of the n-th receiving element as $\mathbf{p}_n \in \mathbb{R}^3,\ n = 1, \ldots, N$. Then, upon considering the position of the first element as a reference point, we have

$$\mathbf{q}_m = \mathbf{q}_1 + x_m^{\mathrm{t}}\mathbf{i}_{\mathrm{t}} + y_m^{\mathrm{t}}\mathbf{j}_{\mathrm{t}}, \quad m = 1, \ldots, M, \tag{1}$$

$$\mathbf{p}_n = \mathbf{p}_1 + x_n^{\mathrm{r}}\mathbf{i}_{\mathrm{r}} + y_n^{\mathrm{r}}\mathbf{j}_{\mathrm{r}}, \quad n = 1, \ldots, N, \tag{2}$$

where $x_m^{\mathrm{t}} = d_{\mathrm{t,x}} \times \mathrm{mod}\,(m-1, M_{\mathrm{x}})$ and $y_m^{\mathrm{t}} = d_{\mathrm{t,y}} \times \lfloor (m-1)/M_{\mathrm{x}} \rfloor$ represent the distances between the m-th element and the first element along the $\mathbf{i}_{\mathrm{t}}$ and $\mathbf{j}_{\mathrm{t}}$ directions, respectively. Furthermore, $d_{\mathrm{t,x}}$ and $d_{\mathrm{t,y}}$ denote the spacings between the adjacent antenna elements in $\mathbf{i}_{\mathrm{t}}$ and $\mathbf{j}_{\mathrm{t}}$ directions, respectively. Similarly, $x_n^{\mathrm{r}} = d_{\mathrm{r,x}} \times \mathrm{mod}\,(n-1, N_{\mathrm{x}})$ and $y_n^{\mathrm{r}} = d_{\mathrm{r,y}} \times \lfloor (n-1)/N_{\mathrm{x}} \rfloor$ represent the distances between the n-th element and the first element along the $\mathbf{i}_{\mathrm{r}}$ and $\mathbf{j}_{\mathrm{r}}$ directions, respectively, while $d_{\mathrm{r,x}}$ and $d_{\mathrm{r,y}}$ denote the spacings between adjacent antenna elements in the $\mathbf{i}_{\mathrm{r}}$ and $\mathbf{j}_{\mathrm{r}}$ directions, respectively.

Furthermore, each radiating element on the transmitting and receiving FIMs can be independently adjusted along their respective normal directions $\mathbf{k}_{\mathrm{t}}$ and $\mathbf{k}_{\mathrm{r}}$, yielding

$$\tilde{\mathbf{q}}_m = \mathbf{q}_m + \zeta_m\mathbf{k}_{\mathrm{t}}, \quad m = 1, \ldots, M, \tag{3}$$

$$\tilde{\mathbf{p}}_n = \mathbf{p}_n + \xi_n\mathbf{k}_{\mathrm{r}}, \quad n = 1, \ldots, N, \tag{4}$$

where ζ_m and ξ_n represent the deformation distances of the m-th transmitting element and the n-th receiving element, respectively. They satisfy $-\tilde{\zeta} \le \zeta_m \le \tilde{\zeta}$ and $-\tilde{\xi} \le \xi_n \le \tilde{\xi}$, with $\tilde{\zeta} \ge 0$ and $\tilde{\xi} \ge 0$ characterizing the maximum range allowed by the unilateral reversible deformation of the transmitting and receiving FIMs, respectively [16]. As a result, the surface shapes of the transmitting FIM at the source and the receiving FIM at the destination are characterized by $\boldsymbol{\zeta} = [\zeta_1, \zeta_2, \ldots, \zeta_M]^T \in \mathbb{R}^M$ and $\boldsymbol{\xi} = [\xi_1, \xi_2, \ldots, \xi_N]^T \in \mathbb{R}^N$.

In this paper, we adopt the multipath propagation model of [18] for characterizing the wireless channels. Moreover, we consider a quasi-static block fading environment and focus our attention on a specific block. Additionally, we consider narrowband transmission over frequency-flat channels. Note that in contrast to conventional MIMO communication systems, the channels in FIM-aided MIMO systems depend on the 3D surface shapes of the transmitting and receiving FIMs. Specifically, let $\mathbf{H}(\boldsymbol{\zeta}, \boldsymbol{\xi}) \in \mathbb{C}^{N \times M}$ denote the MIMO channel spanning from the transmitting FIM to the receiving FIM. Let L represent the number of scattering clusters, each containing G propagation paths. We also assume that all scatterers are located in the far field of the transmitting and receiving FIMs.

Let $\varphi_{l,g}^{\mathrm{t}} \in [0, \pi)$ and $\vartheta_{l,g}^{\mathrm{t}} \in [0, \pi)$ represent the azimuth and elevation angles of departure (AoD), respectively, for the g-th propagation path in the l-th scattering cluster *w.r.t.* the transmitting FIM. Let furthermore $\varphi_{l,g}^{\mathrm{r}} \in [0, \pi)$ and $\vartheta_{l,g}^{\mathrm{r}} \in [0, \pi)$ denote the azimuth and elevation angles of arrival (AoA), respectively, for the g-th propagation path in the l-th scattering cluster *w.r.t.* the receiving FIM. The corresponding propagation direction $\mathbf{o}_{l,g}^{\mathrm{t}} \in \mathbb{R}^3$ and $\mathbf{o}_{l,g}^{\mathrm{r}} \in \mathbb{R}^3$ can be expressed as

$$\mathbf{o}_{l,g}^{\mathrm{t}} = \left[\sin\vartheta_{l,g}^{\mathrm{t}}\cos\varphi_{l,g}^{\mathrm{t}}, \sin\vartheta_{l,g}^{\mathrm{t}}\sin\varphi_{l,g}^{\mathrm{t}}, \cos\vartheta_{l,g}^{\mathrm{t}}\right]^T, \tag{5}$$

$$\mathbf{o}_{l,g}^{\mathrm{r}} = \left[\sin\vartheta_{l,g}^{\mathrm{r}}\cos\varphi_{l,g}^{\mathrm{r}}, \sin\vartheta_{l,g}^{\mathrm{r}}\sin\varphi_{l,g}^{\mathrm{r}}, \cos\vartheta_{l,g}^{\mathrm{r}}\right]^T, \tag{6}$$

respectively, for $g = 1, \ldots, G,\ l = 1, \ldots, L$.

According to (5) and (6), the array steering vectors $\mathbf{a}_{\mathrm{t}}\left(\varphi_{l,g}^{\mathrm{t}}, \vartheta_{l,g}^{\mathrm{t}}\right) \in \mathbb{C}^M$ of the *unmorphed* transmitting FIM and $\mathbf{a}_{\mathrm{r}}\left(\varphi_{l,g}^{\mathrm{r}}, \vartheta_{l,g}^{\mathrm{r}}\right) \in \mathbb{C}^N$ of the *unmorphed* receiving FIM are given by

$$\mathbf{a}_{\mathrm{t}}\left(\varphi_{l,g}^{\mathrm{t}}, \vartheta_{l,g}^{\mathrm{t}}\right) = \Big[1, \ldots, e^{j\kappa\left(x_m^{\mathrm{t}}\left\langle \mathbf{i}_{\mathrm{t}}, \mathbf{o}_{l,g}^{\mathrm{t}}\right\rangle + y_m^{\mathrm{t}}\left\langle \mathbf{j}_{\mathrm{t}}, \mathbf{o}_{l,g}^{\mathrm{t}}\right\rangle\right)}, \ldots, e^{j\kappa\left(x_M^{\mathrm{t}}\left\langle \mathbf{i}_{\mathrm{t}}, \mathbf{o}_{l,g}^{\mathrm{t}}\right\rangle + y_M^{\mathrm{t}}\left\langle \mathbf{j}_{\mathrm{t}}, \mathbf{o}_{l,g}^{\mathrm{t}}\right\rangle\right)}\Big]^T, \tag{7}$$

$$\mathbf{a}_{\mathrm{r}}\left(\varphi_{l,g}^{\mathrm{r}}, \vartheta_{l,g}^{\mathrm{r}}\right) = \Big[1, \ldots, e^{j\kappa\left(x_n^{\mathrm{r}}\left\langle \mathbf{i}_{\mathrm{r}}, \mathbf{o}_{l,g}^{\mathrm{r}}\right\rangle + y_n^{\mathrm{r}}\left\langle \mathbf{j}_{\mathrm{r}}, \mathbf{o}_{l,g}^{\mathrm{r}}\right\rangle\right)}, \ldots, e^{j\kappa\left(x_N^{\mathrm{r}}\left\langle \mathbf{i}_{\mathrm{r}}, \mathbf{o}_{l,g}^{\mathrm{r}}\right\rangle + y_N^{\mathrm{r}}\left\langle \mathbf{j}_{\mathrm{r}}, \mathbf{o}_{l,g}^{\mathrm{r}}\right\rangle\right)}\Big]^T, \tag{8}$$

respectively, where $\kappa = 2\pi/\lambda$ represents the wavenumber, with λ denoting the radio wavelength, $\langle \cdot, \cdot \rangle$ calculates the cosine of the angle between two vectors.

Furthermore, the transmitting and receiving FIMs are capable of imposing additional 3D deformation for fine-tuning the position of each antenna deposited on them. Specifically, the additional multiplicative response components $\mathbf{f}_{\mathrm{t}}\left(\boldsymbol{\zeta}, \varphi_{l,g}^{\mathrm{t}}, \vartheta_{l,g}^{\mathrm{t}}\right) \in \mathbb{C}^M$ and $\mathbf{f}_{\mathrm{r}}\left(\boldsymbol{\xi}, \varphi_{l,g}^{\mathrm{r}}, \vartheta_{l,g}^{\mathrm{r}}\right) \in \mathbb{C}^N$ can be explicitly expressed as

$$\mathbf{f}_{\mathrm{t}}\left(\boldsymbol{\zeta}, \varphi_{l,g}^{\mathrm{t}}, \vartheta_{l,g}^{\mathrm{t}}\right) = \left[1, \ldots, e^{j\kappa\zeta_m\left\langle \mathbf{k}_{\mathrm{t}}, \mathbf{o}_{l,g}^{\mathrm{t}}\right\rangle}, \ldots, e^{j\kappa\zeta_M\left\langle \mathbf{k}_{\mathrm{t}}, \mathbf{o}_{l,g}^{\mathrm{t}}\right\rangle}\right]^T, \tag{9}$$

$$\mathbf{f}_{r}\left(\boldsymbol{\xi}, \varphi_{l,g}^{\mathrm{r}}, \vartheta_{l,g}^{\mathrm{r}}\right) = \left[1, \ldots, e^{j\kappa\xi_n\left\langle \mathbf{k}_{\mathrm{r}}, \mathbf{o}_{l,g}^{\mathrm{r}}\right\rangle}, \ldots, e^{j\kappa\xi_N\left\langle \mathbf{k}_{\mathrm{r}}, \mathbf{o}_{l,g}^{\mathrm{r}}\right\rangle}\right]^T, \tag{10}$$

respectively.

As a result, the array steering vectors $\tilde{\mathbf{a}}_{\mathrm{t}}\left(\boldsymbol{\zeta}, \varphi_{l,g}^{\mathrm{t}}, \vartheta_{l,g}^{\mathrm{t}}\right) \in \mathbb{C}^M$ of the transmitting FIM and $\tilde{\mathbf{a}}_{\mathrm{r}}\left(\boldsymbol{\xi}, \varphi_{l,g}^{\mathrm{r}}, \vartheta_{l,g}^{\mathrm{r}}\right) \in \mathbb{C}^N$ of the receiving FIM can be represented as

$$\tilde{\mathbf{a}}_{\mathrm{t}}\left(\boldsymbol{\zeta}, \varphi_{l,g}^{\mathrm{t}}, \vartheta_{l,g}^{\mathrm{t}}\right) = \mathbf{a}_{\mathrm{t}}\left(\varphi_{l,g}^{\mathrm{t}}, \vartheta_{l,g}^{\mathrm{t}}\right) \odot \mathbf{f}_{\mathrm{t}}\left(\boldsymbol{\zeta}, \varphi_{l,g}^{\mathrm{t}}, \vartheta_{l,g}^{\mathrm{t}}\right), \tag{11}$$

$$\tilde{\mathbf{a}}_{\mathrm{r}}\left(\boldsymbol{\xi}, \varphi_{l,g}^{\mathrm{r}}, \vartheta_{l,g}^{\mathrm{r}}\right) = \mathbf{a}_{\mathrm{r}}\left(\varphi_{l,g}^{\mathrm{r}}, \vartheta_{l,g}^{\mathrm{r}}\right) \odot \mathbf{f}_{\mathrm{r}}\left(\boldsymbol{\xi}, \varphi_{l,g}^{\mathrm{r}}, \vartheta_{l,g}^{\mathrm{r}}\right), \tag{12}$$

for $g = 1, \ldots, G$ and $l = 1, \ldots, L$, where $\odot$ represents the Hadamard product.

By combining (11) and (12), the narrowband MIMO channel $\mathbf{H}(\boldsymbol{\zeta}, \boldsymbol{\xi})$ between the transmitting FIM and the receiving FIM can be written as

$$\mathbf{H}(\boldsymbol{\zeta}, \boldsymbol{\xi}) = \sum_{l=1}^{L}\sum_{g=1}^{G} \varsigma_{l,g}\tilde{\mathbf{a}}_{\mathrm{r}}\left(\boldsymbol{\xi}, \varphi_{l,g}^{\mathrm{r}}, \vartheta_{l,g}^{\mathrm{r}}\right)\tilde{\mathbf{a}}_{\mathrm{t}}^{H}\left(\boldsymbol{\zeta}, \varphi_{l,g}^{\mathrm{t}}, \vartheta_{l,g}^{\mathrm{t}}\right), \tag{13}$$

where $\varsigma_{l,g} \in \mathbb{C},\ g = 1, \ldots, G,\ l = 1, \ldots, L$ represents the complex gain of the g-th propagation path in the l-th scattering cluster. Specifically, $\varsigma_{l,g}$ is assumed to be independent and identically distributed (i.i.d.) CSCG variable, satisfying that $\varsigma_{l,g} \sim \mathcal{CN}\left(0, \rho_l^2/G\right)$, where ρ_l^2 represents the average power of the l-th cluster [19]. Furthermore, let β^2 represent the path loss between the source and the destination. Consequently, we have $\sum_{l=1}^{L}\rho_l^2 = \beta^2$.

For brevity, we define $\mathbf{A}_{\mathrm{t}} \in \mathbb{C}^{M\times LG}$, $\mathbf{F}_{\mathrm{t}}(\boldsymbol{\zeta}) \in \mathbb{C}^{M\times LG}$, $\mathbf{A}_{\mathrm{r}} \in \mathbb{C}^{N\times LG}$, $\mathbf{F}_{\mathrm{r}}(\boldsymbol{\xi}) \in \mathbb{C}^{N\times LG}$, and $\boldsymbol{\varsigma} \in \mathbb{C}^{LG\times LG}$ as

$$\begin{aligned}\mathbf{A}_{\mathrm{t}} \triangleq &\left[\mathbf{a}_{\mathrm{t}}\left(\varphi_{1,1}^{\mathrm{t}}, \vartheta_{1,1}^{\mathrm{t}}\right), \ldots, \mathbf{a}_{\mathrm{t}}\left(\varphi_{1,G}^{\mathrm{t}}, \vartheta_{1,G}^{\mathrm{t}}\right), \ldots,\right.\\ &\left.\mathbf{a}_{\mathrm{t}}\left(\varphi_{L,1}^{\mathrm{t}}, \vartheta_{L,1}^{\mathrm{t}}\right), \ldots, \mathbf{a}_{\mathrm{t}}\left(\varphi_{L,G}^{\mathrm{t}}, \vartheta_{L,G}^{\mathrm{t}}\right)\right],\end{aligned} \tag{14}$$

$$\begin{aligned}\mathbf{F}_{\mathrm{t}}(\boldsymbol{\zeta}) \triangleq &\left[\mathbf{f}_{\mathrm{t}}\left(\boldsymbol{\zeta}, \varphi_{1,1}^{\mathrm{t}}, \vartheta_{1,1}^{\mathrm{t}}\right), \ldots, \mathbf{f}_{\mathrm{t}}\left(\boldsymbol{\zeta}, \varphi_{1,G}^{\mathrm{t}}, \vartheta_{1,G}^{\mathrm{t}}\right), \ldots,\right.\\ &\left.\mathbf{f}_{\mathrm{t}}\left(\boldsymbol{\zeta}, \varphi_{L,1}^{\mathrm{t}}, \vartheta_{L,1}^{\mathrm{t}}\right), \ldots, \mathbf{f}_{\mathrm{t}}\left(\boldsymbol{\zeta}, \varphi_{L,G}^{\mathrm{t}}, \vartheta_{L,G}^{\mathrm{t}}\right)\right],\end{aligned} \tag{15}$$

$$\begin{aligned}\mathbf{A}_{\mathrm{r}} \triangleq &\left[\mathbf{a}_{r}\left(\varphi_{1,1}^{\mathrm{r}}, \vartheta_{1,1}^{\mathrm{r}}\right), \ldots, \mathbf{a}_{r}\left(\varphi_{1,G}^{\mathrm{r}}, \vartheta_{1,G}^{\mathrm{r}}\right), \ldots,\right.\\ &\left.\mathbf{a}_{r}\left(\varphi_{L,1}^{\mathrm{r}}, \vartheta_{L,1}^{\mathrm{r}}\right), \ldots, \mathbf{a}_{r}\left(\varphi_{L,G}^{\mathrm{r}}, \vartheta_{L,G}^{\mathrm{r}}\right)\right],\end{aligned} \tag{16}$$

$$\begin{aligned}\mathbf{F}_{\mathrm{r}}(\boldsymbol{\xi}) \triangleq &\left[\mathbf{f}_{r}\left(\boldsymbol{\xi}, \varphi_{1,1}^{\mathrm{r}}, \vartheta_{1,1}^{\mathrm{r}}\right), \ldots, \mathbf{f}_{r}\left(\boldsymbol{\xi}, \varphi_{1,G}^{\mathrm{r}}, \vartheta_{1,G}^{\mathrm{r}}\right), \ldots,\right.\\ &\left.\mathbf{f}_{r}\left(\boldsymbol{\xi}, \varphi_{L,1}^{\mathrm{r}}, \vartheta_{L,1}^{\mathrm{r}}\right), \ldots, \mathbf{f}_{\mathrm{r}}\left(\boldsymbol{\xi}, \varphi_{L,G}^{\mathrm{r}}, \vartheta_{L,G}^{\mathrm{r}}\right)\right],\end{aligned} \tag{17}$$

$$\boldsymbol{\varsigma} \triangleq \mathrm{diag}\left(\varsigma_{1,1}, \ldots, \varsigma_{1,G}, \ldots, \varsigma_{L,1}, \ldots, \varsigma_{L,G}\right). \tag{18}$$

Hence, the matrix form of the FIM-aided MIMO channel in (13) is given by

$$\mathbf{H}(\boldsymbol{\zeta}, \boldsymbol{\xi}) = \left[\mathbf{A}_{\mathrm{r}} \odot \mathbf{F}_{\mathrm{r}}(\boldsymbol{\xi})\right]\boldsymbol{\varsigma}\left[\mathbf{A}_{\mathrm{t}} \odot \mathbf{F}_{\mathrm{t}}(\boldsymbol{\zeta})\right]^H. \tag{19}$$

Furthermore, let $\mathbf{T} \in \mathbb{C}^{M\times M}$ denote the transmit signal's covariance matrix, satisfying $\mathbf{T} \succeq \mathbf{0}$ and $\mathrm{tr}(\mathbf{T}) \le P_{\mathrm{t}}$, with P_{t} representing the power budget at the transmitter. Hence, the MIMO channel capacity measured in bits per second per Hertz (bps/Hz) is given by

$$\max_{\mathbf{T}, \boldsymbol{\zeta}, \boldsymbol{\xi}} \underbrace{\log_2 \det\left(\mathbf{I}_N + \frac{1}{\sigma^2}\mathbf{H}(\boldsymbol{\zeta}, \boldsymbol{\xi})\mathbf{T}\mathbf{H}^H(\boldsymbol{\zeta}, \boldsymbol{\xi})\right)}_{C}. \tag{20}$$

In conventional MIMO communication systems relying on RAAs ($\boldsymbol{\zeta} = \mathbf{0}$ and $\boldsymbol{\xi} = \mathbf{0}$), the capacity is fully determined by the channel matrix $\mathbf{H}(\mathbf{0}, \mathbf{0})$. By contrast, for MIMO communications between a pair of FIMs, the channel capacity $\mathbf{H}(\boldsymbol{\zeta}, \boldsymbol{\xi})$ also depends on the 3D surface-shape configurations of the transmitting FIM $\boldsymbol{\zeta}$ and receiving FIM $\boldsymbol{\xi}$, which provide extra design DoFs for further improving the channel capacity in a more energy-efficient way.

III. Joint Surface Shape Morphing and Transmit Optimization for Capacity Maximization

A. Problem Formulation

In this paper, we aim for maximizing the capacity of a MIMO channel between a pair of FIMs by jointly optimizing the 3D surface shapes $\boldsymbol{\zeta}$ and $\boldsymbol{\xi}$ of the transmitting and receiving FIMs, as well as the transmit covariance matrix $\mathbf{T}$, subject to the morphing range of these two FIMs and a total power constraint at the source. Specifically, the joint optimization problem is formulated as

$$\max_{\mathbf{T}, \boldsymbol{\zeta}, \boldsymbol{\xi}} \quad \log_2 \det\left(\mathbf{I}_N + \frac{1}{\sigma^2}\mathbf{H}(\boldsymbol{\zeta}, \boldsymbol{\xi})\mathbf{T}\mathbf{H}^H(\boldsymbol{\zeta}, \boldsymbol{\xi})\right) \tag{21a}$$

$$\text{s.t.} \quad \mathrm{tr}(\mathbf{T}) \le P_{\mathrm{t}}, \quad \mathbf{T} \succeq \mathbf{0}, \tag{21b}$$

$$\boldsymbol{\zeta} = \left[\zeta_1, \zeta_2, \ldots, \zeta_M\right]^T, \tag{21c}$$

$$\boldsymbol{\xi} = \left[\xi_1, \xi_2, \ldots, \xi_N\right]^T, \tag{21d}$$

$$-\tilde{\zeta} \le \zeta_m \le \tilde{\zeta}, \quad m = 1, \ldots, M, \tag{21e}$$

$$-\tilde{\xi} \le \xi_n \le \tilde{\xi}, \quad n = 1, \ldots, N, \tag{21f}$$

where (21b) characterizes the transmit power constraint, while (21c) – (21f) represent the constraints on adjusting the morphing range of each antenna on the transmitting and receiving FIMs.

Note that problem (21) is challenging to solve optimally, because the objective function in (21a) is non-concave *w.r.t.* the surface-shape configurations $\boldsymbol{\zeta}$ and $\boldsymbol{\xi}$ of the transmitting and receiving FIMs. Moreover, $\boldsymbol{\zeta}$ and $\boldsymbol{\xi}$ are tightly coupled with the transmit covariance matrix $\mathbf{T}$ in the objective function (21a). In the next subsection, we will decompose problem (21) into two subproblems and propose an efficient BCD algorithm to sub-optimally solve it.

B. The Proposed Block Coordinate Descent Algorithm

Specifically, the BCD iteratively solves two subproblems for optimizing the transmit covariance matrix $\mathbf{T}$ or the surface shapes of the transmitting and receiving FIMs $\{\boldsymbol{\zeta},\ \boldsymbol{\xi}\}$ respectively, with the other set of variables being fixed.

1) Transmit Covariance Optimization with Given $\left\{\hat{\boldsymbol{\zeta}},\ \hat{\boldsymbol{\xi}}\right\}$*:* In this subproblem, we aim for optimizing the transmit covariance matrix $\mathbf{T}$ given a tentative surface-shape configuration $\left\{\hat{\boldsymbol{\zeta}},\ \hat{\boldsymbol{\xi}}\right\}$ for the transmitting and receiving FIMs. In this case, the MIMO channel $\mathbf{H}\left(\hat{\boldsymbol{\zeta}},\ \hat{\boldsymbol{\xi}}\right)$ between the source and the destination is determined by (19), and the original problem in (21) simplifies to a conventional MIMO system optimization problem, with the optimal $\mathbf{T}$ being determined by the eigenmode transmission [17].

Specifically, let $\mathbf{H}^H\left(\hat{\boldsymbol{\zeta}},\ \hat{\boldsymbol{\xi}}\right)\mathbf{H}\left(\hat{\boldsymbol{\zeta}},\ \hat{\boldsymbol{\xi}}\right) = \mathbf{U}\boldsymbol{\Lambda}\mathbf{U}^H$ denote the eigenvalue decomposition of $\mathbf{H}^H\left(\hat{\boldsymbol{\zeta}},\ \hat{\boldsymbol{\xi}}\right)\mathbf{H}\left(\hat{\boldsymbol{\zeta}},\ \hat{\boldsymbol{\xi}}\right)$, with $\boldsymbol{\Lambda} = \operatorname{diag}\left(\lambda_1^2, \lambda_2^2, \ldots, \lambda_M^2\right) \in \mathbb{R}^{M\times M}$ representing the eigenvalue matrix. The optimal transmit covariance matrix $\mathbf{T}^o$ is thus given by $\mathbf{T}^o = \mathbf{U}\mathbf{P}^o\mathbf{U}^H$, where we have $\mathbf{P}^o = \operatorname{diag}\left(p_1^o, p_2^o, \ldots, p_M^o\right) \in \mathbb{R}^{M\times M}$, and p_m^o represents the amount of power allocated to the m-th data stream. Specifically, the optimal value of p_m^o can be obtained using the water-filling strategy, which gives $p_m^o = \max\left(\mu - \sigma^2/\lambda_m^2, 0\right),\ m = 1, \ldots, M$, where μ is a threshold such that $\sum_{m=1}^{M} p_m^o = P_{\mathrm{t}}$.

2) Surface-Shape Morphing with Given $\hat{\mathbf{T}}$*:* Next, we aim for obtaining the optimal surface-shape configuration $\{\boldsymbol{\zeta},\ \boldsymbol{\xi}\}$ in (21) for a given transmit covariance matrix $\hat{\mathbf{T}}$. Specifically, substituting $\hat{\mathbf{T}}$ into (21) yields

$$\max_{\boldsymbol{\zeta},\ \boldsymbol{\xi}} \quad \log_2\det\left(\mathbf{I}_N + \frac{1}{\sigma^2}\mathbf{H}\left(\boldsymbol{\zeta},\boldsymbol{\xi}\right)\hat{\mathbf{T}}\mathbf{H}^H\left(\boldsymbol{\zeta},\boldsymbol{\xi}\right)\right) \tag{22a}$$

$$\text{s.t.} \quad \text{(21c), (21d), (21e), (21f).} \tag{22b}$$

Since an optimal solution to (22) is still difficult to obtain, instead we leverage the GA algorithm to find a sub-optimal solution. Specifically, given the surface shapes of the transmitting and receiving FIMs obtained from the previous iteration, we can adjust their surface-shape configurations towards the direction of the gradient for gradually increasing the channel capacity. The GA algorithm involves two major steps: *i)* gradient calculation, and *ii)* surface-shape update.

a) **Gradient Calculation:** The GA method requires calculating the gradients of the objective function C *w.r.t.* the surface-shape configurations $\boldsymbol{\zeta}$ and $\boldsymbol{\xi}$ of the transmitting and receiving FIMs, which can be obtained by using *Propositions 1 and 2*, respectively.

***Proposition** 1:* The gradient of C *w.r.t.* $\boldsymbol{\xi}$, i.e., $\nabla_{\boldsymbol{\xi}}C$, and the gradient of C *w.r.t.* $\boldsymbol{\zeta}$, i.e., $\nabla_{\boldsymbol{\zeta}}C$, are given by

$$\nabla_{\boldsymbol{\xi}}C = -\frac{2}{\ln 2}\operatorname{Diag}\left[\mathbf{B}_{\mathrm{r}}^{-1}\odot\Im\left(\mathbf{S}_{\mathrm{r}}\right)\right], \tag{23}$$

$$\nabla_{\boldsymbol{\zeta}}C = -\frac{2}{\ln 2}\operatorname{Diag}\left[\mathbf{B}_{\mathrm{t}}^{-1}\odot\Im\left(\mathbf{S}_{\mathrm{t}}\right)\right], \tag{24}$$

where the matrices $\mathbf{S}_{\mathrm{r}} \in \mathbb{C}^{N\times N}$, $\mathbf{B}_{\mathrm{r}} \in \mathbb{C}^{N\times N}$, $\mathbf{O}_{\mathrm{t}} \in \mathbb{C}^{LG\times LG}$, $\mathbf{K}_{\mathrm{r}} \in \mathbb{R}^{LG\times LG}$, $\mathbf{S}_{\mathrm{t}} \in \mathbb{C}^{M\times M}$, $\mathbf{B}_{\mathrm{t}} \in \mathbb{C}^{M\times M}$, $\mathbf{O}_{\mathrm{r}} \in \mathbb{C}^{LG\times LG}$, and $\mathbf{K}_{\mathrm{t}} \in \mathbb{R}^{LG\times LG}$ are defined by

$$\mathbf{S}_{\mathrm{r}} \triangleq \left[\mathbf{A}_{\mathrm{r}}\odot\mathbf{F}_{\mathrm{r}}\left(\boldsymbol{\xi}\right)\right]\mathbf{K}_{\mathrm{r}}\mathbf{O}_{\mathrm{t}}\left[\mathbf{A}_{\mathrm{r}}\odot\mathbf{F}_{\mathrm{r}}\left(\boldsymbol{\xi}\right)\right]^H, \tag{25}$$

$$\mathbf{B}_{\mathrm{r}} \triangleq \mathbf{I}_N + \left[\mathbf{A}_{\mathrm{r}}\odot\mathbf{F}_{\mathrm{r}}\left(\boldsymbol{\xi}\right)\right]\mathbf{O}_{\mathrm{t}}\left[\mathbf{A}_{\mathrm{r}}\odot\mathbf{F}_{\mathrm{r}}\left(\boldsymbol{\xi}\right)\right]^H, \tag{26}$$

$$\mathbf{O}_{\mathrm{t}} \triangleq \frac{1}{\sigma^2}\boldsymbol{\varsigma}\left[\mathbf{A}_{\mathrm{t}}\odot\mathbf{F}_{\mathrm{t}}\left(\boldsymbol{\zeta}\right)\right]^H\hat{\mathbf{T}}\left[\mathbf{A}_{\mathrm{t}}\odot\mathbf{F}_{\mathrm{t}}\left(\boldsymbol{\zeta}\right)\right]\boldsymbol{\varsigma}^H, \tag{27}$$

$$\begin{aligned}\mathbf{K}_{\mathrm{r}} \triangleq &\operatorname{diag}\left(\kappa\left\langle\mathbf{k}_{\mathrm{r}}, \mathbf{o}_{1,1}^{\mathrm{r}}\right\rangle, \ldots, \kappa\left\langle\mathbf{k}_{\mathrm{r}}, \mathbf{o}_{1,G}^{\mathrm{r}}\right\rangle, \ldots,\right.\\ &\left.\kappa\left\langle\mathbf{k}_{\mathrm{r}}, \mathbf{o}_{L,1}^{\mathrm{r}}\right\rangle, \ldots, \kappa\left\langle\mathbf{k}_{\mathrm{r}}, \mathbf{o}_{L,G}^{\mathrm{r}}\right\rangle\right),\end{aligned} \tag{28}$$

$$\mathbf{S}_{\mathrm{t}} \triangleq \hat{\mathbf{T}}\left[\mathbf{A}_{\mathrm{t}}\odot\mathbf{F}_{\mathrm{t}}\left(\boldsymbol{\zeta}\right)\right]\mathbf{K}_{\mathrm{t}}\mathbf{O}_{\mathrm{r}}\left[\mathbf{A}_{\mathrm{t}}\odot\mathbf{F}_{\mathrm{t}}\left(\boldsymbol{\zeta}\right)\right]^H, \tag{29}$$

$$\mathbf{B}_{\mathrm{t}} \triangleq \mathbf{I}_M + \hat{\mathbf{T}}\left[\mathbf{A}_{\mathrm{t}}\odot\mathbf{F}_{\mathrm{t}}\left(\boldsymbol{\zeta}\right)\right]\mathbf{O}_{\mathrm{r}}\left[\mathbf{A}_{\mathrm{t}}\odot\mathbf{F}_{\mathrm{t}}\left(\boldsymbol{\zeta}\right)\right]^H, \tag{30}$$

$$\mathbf{O}_{\mathrm{r}} \triangleq \frac{1}{\sigma^2}\boldsymbol{\varsigma}^H\left[\mathbf{A}_{\mathrm{r}}\odot\mathbf{F}_{\mathrm{r}}\left(\boldsymbol{\xi}\right)\right]^H\left[\mathbf{A}_{\mathrm{r}}\odot\mathbf{F}_{\mathrm{r}}\left(\boldsymbol{\xi}\right)\right]\boldsymbol{\varsigma}, \tag{31}$$

$$\begin{aligned}\mathbf{K}_{\mathrm{t}} \triangleq &\operatorname{diag}\left(\kappa\left\langle\mathbf{k}_{\mathrm{t}}, \mathbf{o}_{1,1}^{\mathrm{t}}\right\rangle, \ldots, \kappa\left\langle\mathbf{k}_{\mathrm{t}}, \mathbf{o}_{1,G}^{\mathrm{t}}\right\rangle, \ldots,\right.\\ &\left.\kappa\left\langle\mathbf{k}_{\mathrm{t}}, \mathbf{o}_{L,1}^{\mathrm{t}}\right\rangle, \ldots, \kappa\left\langle\mathbf{k}_{\mathrm{t}}, \mathbf{o}_{L,G}^{\mathrm{t}}\right\rangle\right),\end{aligned} \tag{32}$$

respectively.

Proof: Please refer to Appendix A. ■

b) **Surface-Shape Morphing:** At each iteration, the 3D surface shapes of the transmitting and receiving FIMs are updated by

$$\boldsymbol{\zeta} \leftarrow \boldsymbol{\zeta} + \epsilon\nabla_{\boldsymbol{\zeta}}C, \tag{33}$$

$$\boldsymbol{\xi} \leftarrow \boldsymbol{\xi} + \epsilon\nabla_{\boldsymbol{\xi}}C, \tag{34}$$

where $\epsilon > 0$ represents the step size, which is determined by applying a backtracking line search [14].

Additionally, a projection process is imposed on the positions obtained from (33) and (34) for scaling them into the allowable morphing ranges of the FIMs, i.e.,

$$\zeta_m = \max\left(\min\left(\zeta_m, \tilde{\zeta}\right), -\tilde{\zeta}\right), \quad m = 1, \ldots, M, \tag{35}$$

$$\xi_n = \max\left(\min\left(\xi_n, \tilde{\xi}\right), -\tilde{\xi}\right), \quad n = 1, \ldots, N. \tag{36}$$

By continually updating the surface shapes according to (33) and (34), the optimal surface shapes $\boldsymbol{\zeta}^{\mathrm{o}}$ and $\boldsymbol{\xi}^{\mathrm{o}}$ of the transmitting and receiving FIMs can be obtained. The proposed BCD algorithm is guaranteed to converge to at least a locally optimal solution for two reasons. *Firstly*, the objective function value in (21a) is non-decreasing as the iteration proceeds by selecting an appropriate step size according to the backtracking line search. *Secondly*, the objective function is upper bounded due to the power constraint in (21b).

IV. Numerical Results

We consider a 3D Cartesian coordinate system, where the locations of the reference antennas at the source and destination are set as $(0\text{ m}, 0\text{ m}, 10\text{ m})$ and $(0\text{ m}, 100\text{ m}, 0\text{ m})$, respectively. Both the source and destination are equipped with an FIM, with $M = M_{\mathrm{x}}M_{\mathrm{y}}$ antennas at the source and $N = N_{\mathrm{x}}N_{\mathrm{y}}$ antennas at the destination. The antenna spacings at the source and destination are $\{d_{\mathrm{t,x}},\ d_{\mathrm{t,y}}\}$ and $\{d_{\mathrm{r,x}},\ d_{\mathrm{r,y}}\}$, respectively. In our simulations, we set $d_{\mathrm{t,x}} = d_{\mathrm{t,y}} = d_{\mathrm{r,x}} = d_{\mathrm{r,y}} = \lambda/2$. The FIMs' orientations are configured by setting $\varphi_{\mathrm{t}} = \varphi_{\mathrm{r}} = \pi/2,\ \vartheta_{\mathrm{t}} = \vartheta_{\mathrm{r}} = 3\pi/4$, unless otherwise specified.

Furthermore, the distance-dependent path loss of the wireless channel is modeled as $\beta^2 = \beta_0^2\left(d/d_0\right)^{-\alpha}$ [20], where $\beta_0^2 = -60$ dB denotes the path loss at the reference distance

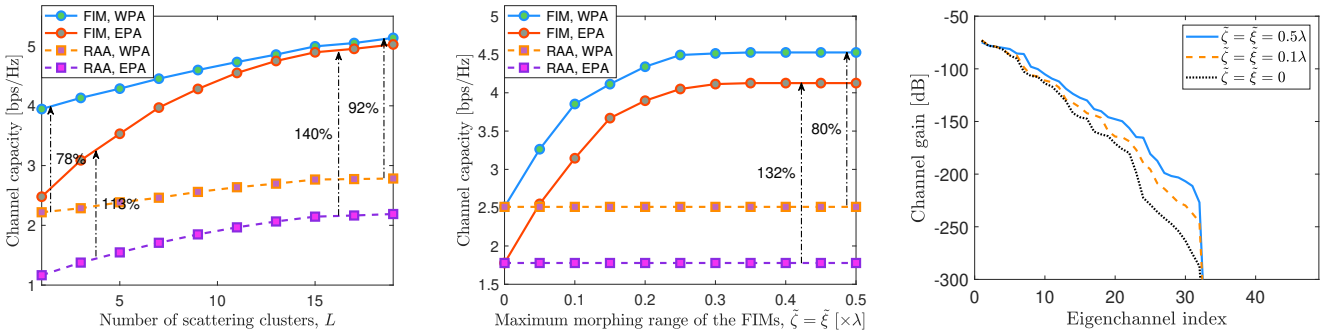

(a) (b) (c)

Fig. 2. (a) Channel capacity C versus the number of scattering clusters L; (b) Channel capacity C versus the morphing range of the FIMs $\tilde{\zeta} = \tilde{\xi}$; (c) Channel gain under different values of the maximum morphing range.

of $d_0 = 1$ m, and $\alpha = 2.2$ is the path loss exponent used in our simulations. The propagation environment consists of L scattering clusters, each containing G propagation paths. We assume that all scatterers experience the same channel gain, resulting in $\rho_l^2 = \beta^2/L$ for $l = 1, \ldots, L$. Within the l-th cluster, the G azimuth and elevation AoDs, $\varphi_{l,g}^{\mathrm{t}}$ and $\vartheta_{l,g}^{\mathrm{t}}$, are assumed to be randomly distributed with mean cluster angles of φ_l^{t} and ϑ_l^{t} respectively, and constant angular spreads of $\sigma_\varphi^{\mathrm{t}}$ and $\sigma_\vartheta^{\mathrm{t}}$, respectively. Similarly, the G azimuth and elevation AoAs, $\varphi_{l,g}^{\mathrm{r}}$ and $\vartheta_{l,g}^{\mathrm{r}}$, within the l-th cluster are randomly distributed around the mean cluster angles of φ_l^{r} and ϑ_l^{r}, with angular spreads of $\sigma_\varphi^{\mathrm{r}}$ and $\sigma_\vartheta^{\mathrm{r}}$, respectively. We assume that the L cluster centers are uniformly distributed, satisfying $\varphi_l^{\mathrm{t}},\ \vartheta_l^{\mathrm{t}},\ \varphi_l^{\mathrm{r}},\ \vartheta_l^{\mathrm{r}} \sim \mathcal{U}[0, \pi)$ for $l = 1, \ldots, L$. For simplicity, we further assume $\sigma_\varphi^{\mathrm{t}} = \sigma_\varphi^{\mathrm{r}} \triangleq \sigma_\varphi$ and $\sigma_\vartheta^{\mathrm{t}} = \sigma_\vartheta^{\mathrm{r}} \triangleq \sigma_\vartheta$. Moreover, the system operates at 28 GHz with a bandwidth of 100 MHz. Assuming a noise power spectral density of -174 dBm/Hz yields an average noise power of $\sigma^2 = -94$ dBm.

Moreover, four transmission schemes are considered for evaluating the performance of the FIM, namely *1)* **FIM, WPA:** A pair of FIMs with optimized surface shapes are utilized as transceivers, and the water-filling power allocation is used. *2)* **FIM, EPA:** The equal power allocation scheme is utilized at the source. The transmitting and receiving FIM surface shapes are updated by using the GA method. *3)* **RAA, WPA [1]:** Conventional RAAs are employed, while the classic water-filling power allocation is utilized at the source. *4)* **RAA, EPA [1]:** The equal power allocation is utilized at the conventional RAA-based MIMO transmitter. Additionally, for the proposed BCD algorithm, the maximum tolerable number of iterations is set to 50, and the convergence threshold in terms of the fractional increase in channel capacity is set to -30 dB. All simulation results are obtained by averaging over 100 independent channel realizations.

Furthermore, Fig. 2a examines the performance as the number of scattering clusters in the environment increases. The downlink transmit power constraint is set to $P_{\mathrm{t}} = 10$ dBm. It is demonstrated that as L increases, the MIMO channel capacity improves since the signal components from multiple propagation paths are more likely to form a favorable profile across the array. Moreover, the FIMs outperform conventional RAAs by morphing their surface shapes to find the optimal configurations that experience shallow fading. Notably, the performance gain offered by the FIMs becomes more significant as the number of scattering clusters increases. Specifically, when the number of clusters increases from $L = 1$ to $L = 19$ the performance gain increases from 78% to 92%. This indicates that multipath propagation plays a crucial role in FIM-aided wireless communications.

Fig. 2b plots the channel capacity of different schemes as the morphing ranges of the FIMs increase. We assume that there are $L = 8$ scattering clusters. For simplicity, we also assume $\tilde{\zeta} = \tilde{\xi}$. Note that a conventional RAA is a special case of an FIM when $\tilde{\zeta} = \tilde{\xi} = 0$. Observe from Fig. 2b that as $\tilde{\zeta}$ and $\tilde{\xi}$ increase, the transmitting and receiving FIMs exhibit increased flexibility to adapt their 3D surface shapes, thus gradually increasing the channel capacity. When the classic water-filling power allocation is utilized, the FIMs with a morphing range of $\tilde{\zeta} = \tilde{\xi} = \lambda/2$ could improve the MIMO channel capacity by about 80%. Although the equal power allocation suffers from a moderate capacity penalty when the CSI is only available at the destination, the performance gain from morphing the surface shapes of FIMs increases to 132%. Nevertheless, we observe that further increasing the morphing range leads to diminishing returns.

Finally, we demonstrate the capability of FIMs for morphing their surface shapes. Specifically, a pair of FIMs having 7×7 square antenna arrays are deployed at the source and destination. When considering a maximum morphing range of $\tilde{\zeta} = \tilde{\xi} = 0.1\lambda$. It is demonstrated that the FIMs are capable of morphing their surface shapes by positioning all elements to improve the channel gain. As shown in Fig. 2(c), weak eigenchannels are enhanced by over 40 dB compared to traditional RAAs. Furthermore, we increase the maximum morphing range of the transmitting and receiving FIMs to $\tilde{\zeta} = \tilde{\xi} = 0.5\lambda$. With a larger space to morph their surface shapes, the eigenchannel channel gain is further increased by about 20 dB.

V. Conclusions

In this paper, the FIM technology that has the capability of morphing its 3D surface shape was utilized as MIMO transceivers to enhance the channel capacity. Specifically, a capacity maximization problem was formulated and addressed by developing a customized BCD method for iteratively optimizing the transmit covariance matrix and the 3D surface

shapes of the transmitting and receiving FIMs. Numerical results validated the significant capacity improvement gleaned from morphing the surface shapes of the FIMs compared to the conventional MIMO systems relying on RAAs. Notably, the performance gains become even more pronounced as the maximum morphing range of the FIM and the number of propagation paths increase. Despite the remarkable performance gains achieved by dynamically morphing the 3D surface shapes of FIMs, further research is required to address challenges such as channel estimation.

Appendix A
Proof of Proposition 1

First, the channel capacity C in (20) can be rewritten as $C = \log_2 \det \mathbf{B}_{\mathrm{r}}$. According to *Eq. (3.60)* of [21], the differential of the logarithm of the determinant is given by $dC = \frac{1}{\ln 2}\mathrm{tr}\left(\mathbf{B}_{\mathrm{r}}^{-1} d\mathbf{B}_{\mathrm{r}}\right)$. Furthermore, we have

$$\begin{aligned} d\mathbf{B}_{\mathrm{r}} &\overset{(a)}{=} d\left[\mathbf{A}_{\mathrm{r}} \odot \mathbf{F}_{\mathrm{r}}\left(\boldsymbol{\xi}\right)\right] \mathbf{O}_{\mathrm{t}} \left[\mathbf{A}_{\mathrm{r}} \odot \mathbf{F}_{\mathrm{r}}\left(\boldsymbol{\xi}\right)\right]^H \\ &\quad + \left[\mathbf{A}_{\mathrm{r}} \odot \mathbf{F}_{\mathrm{r}}\left(\boldsymbol{\xi}\right)\right] \mathbf{O}_{\mathrm{t}} d\left[\mathbf{A}_{\mathrm{r}} \odot \mathbf{F}_{\mathrm{r}}\left(\boldsymbol{\xi}\right)\right]^H \\ &\overset{(b)}{=} \left[\mathbf{A}_{\mathrm{r}} \odot d\mathbf{F}_{\mathrm{r}}\left(\boldsymbol{\xi}\right)\right] \mathbf{O}_{\mathrm{t}} \left[\mathbf{A}_{\mathrm{r}} \odot \mathbf{F}_{\mathrm{r}}\left(\boldsymbol{\xi}\right)\right]^H \\ &\quad + \left[\mathbf{A}_{\mathrm{r}} \odot \mathbf{F}_{\mathrm{r}}\left(\boldsymbol{\xi}\right)\right] \mathbf{O}_{\mathrm{t}} \left[\mathbf{A}_{\mathrm{r}} \odot d\mathbf{F}_{\mathrm{r}}\left(\boldsymbol{\xi}\right)\right]^H, \end{aligned} \tag{37}$$

where (a) holds due to $d\left(\mathbf{AB}\right) = d\left(\mathbf{A}\right)\mathbf{B} + \mathbf{A}d\left(\mathbf{B}\right)$, while (b) holds due to $d\left(\mathbf{A} \odot \mathbf{B}\right) = d\left(\mathbf{A}\right) \odot \mathbf{B} + \mathbf{A} \odot d\left(\mathbf{B}\right)$.

Hence, the partial derivative of the matrix $\mathbf{F}_{\mathrm{r}}\left(\boldsymbol{\xi}\right)$ *w.r.t.* the deformation distance ξ_n of the n-th receiving element is given by

$$\frac{\partial}{\partial \xi_n}\mathbf{F}_{\mathrm{r}}\left(\boldsymbol{\xi}\right) = j\tilde{\mathbf{F}}_n^{\mathrm{r}}\left(\boldsymbol{\xi}\right)\mathbf{K}_{\mathrm{r}}, \quad n = 1, \ldots, N, \tag{38}$$

where $\tilde{\mathbf{F}}_n^{\mathrm{r}}\left(\boldsymbol{\xi}\right) \in \mathbb{C}^{N \times LG}$ is defined as

$$\tilde{\mathbf{F}}_n^{\mathrm{r}}\left(\boldsymbol{\xi}\right) = \left[\mathbf{0}_{(n-1)\times LG};\ \left[\mathbf{F}_{\mathrm{r}}\left(\boldsymbol{\xi}\right)\right]_{n,:};\ \mathbf{0}_{(N-n)\times LG}\right]. \tag{39}$$

Substituting (38) into (37), we arrive at

$$\begin{aligned} \frac{\partial}{\partial \xi_n}\mathbf{B}_{\mathrm{r}} &= \left(\mathbf{A}_{\mathrm{r}} \odot j\tilde{\mathbf{F}}_{\mathrm{r}}\left(\boldsymbol{\xi}\right)\mathbf{K}_{\mathrm{r}}\right) \mathbf{O}_{\mathrm{t}} \left(\mathbf{A}_{\mathrm{r}} \odot \mathbf{F}_{\mathrm{r}}\left(\boldsymbol{\xi}\right)\right)^H \\ &\quad + \left(\mathbf{A}_{\mathrm{r}} \odot \mathbf{F}_{\mathrm{r}}\left(\boldsymbol{\xi}\right)\right) \mathbf{O}_{\mathrm{t}} \left(\mathbf{A}_{\mathrm{r}} \odot j\tilde{\mathbf{F}}_{\mathrm{r}}\left(\boldsymbol{\xi}\right)\mathbf{K}_{\mathrm{r}}\right)^H \\ &= -2\Im\left(\tilde{\mathbf{S}}_n^{\mathrm{r}}\right), \quad n = 1, \ldots, N, \end{aligned} \tag{40}$$

where $\tilde{\mathbf{S}}_n^{\mathrm{r}} \in \mathbb{C}^{N \times N}$ is defined as

$$\tilde{\mathbf{S}}_n^{\mathrm{r}} = \begin{bmatrix} \mathbf{0}_{(n-1)\times(n-1)} & \mathbf{0}_{(n-1)\times 1} & \mathbf{0}_{(n-1)\times(N-n)} \\ \mathbf{0}_{1\times(n-1)} & \left[\mathbf{S}_{\mathrm{r}}\right]_{n,n} & \mathbf{0}_{1\times(N-n)} \\ \mathbf{0}_{(N-n)\times(n-1)} & \mathbf{0}_{(N-n)\times 1} & \mathbf{0}_{(N-n)\times(N-n)} \end{bmatrix}. \tag{41}$$

Substituting (40) into dC and collecting N partial derivatives into a matrix, the proof of (23) is completed. Rewriting the channel capacity as $C = \log_2 \det \mathbf{B}_{\mathrm{t}}$, the proof of (24) is completed.

Acknowledgments

This research is supported by the Ministry of Education, Singapore, under its MOE Tier 2 (Award number T2EP50124-0032) and National Research Foundation, Singapore, and Infocomm Media Development Authority under its Future Communications Research & Development Programme FCP-NTU-RG-2024-025.

References

[1] A. Goldsmith, S. Jafar, N. Jindal, and S. Vishwanath, "Capacity limits of MIMO channels," *IEEE J. Sel. Areas Commun.*, vol. 21, no. 5, pp. 684–702, Jun. 2003.

[2] L. Zheng and D. Tse, "Diversity and multiplexing: a fundamental tradeoff in multiple-antenna channels," *IEEE Trans. Inf. Theory*, vol. 49, no. 5, pp. 1073–1096, May 2003.

[3] T. L. Marzetta, "Noncooperative cellular wireless with unlimited numbers of base station antennas," *IEEE Trans. Wireless Commun.*, vol. 9, no. 11, pp. 3590–3600, Nov. 2010.

[4] H. Lu and Y. Zeng, "Communicating with extremely large-scale array/surface: Unified modeling and performance analysis," *IEEE Trans. Wireless Commun.*, vol. 21, no. 6, pp. 4039–4053, Jun. 2022.

[5] J. An, C. Yuen, L. Dai, M. Di Renzo, M. Debbah, and L. Hanzo, "Near-field communications: Research advances, potential, and challenges," *IEEE Wireless Commun.*, vol. 31, no. 3, pp. 100–107, Jun. 2024.

[6] J. An, M. Debbah, T. J. Cui, Z. N. Chen, and C. Yuen, "Emerging technologies in intelligent metasurfaces: Shaping the future of wireless communications," 2024. [Online]. Available: https://arxiv.org/abs/2411.19754

[7] M. Di Renzo, A. Zappone, M. Debbah, M.-S. Alouini, C. Yuen, J. de Rosny, and S. Tretyakov, "Smart radio environments empowered by reconfigurable intelligent surfaces: How it works, state of research, and the road ahead," *IEEE J. Sel. Areas Commun.*, vol. 38, no. 11, pp. 2450–2525, Nov. 2020.

[8] J. An, C. Xu, Q. Wu, D. W. K. Ng, M. D. Renzo, C. Yuen, and L. Hanzo, "Codebook-based solutions for reconfigurable intelligent surfaces and their open challenges," *IEEE Wireless Commun.*, vol. 31, no. 2, pp. 134–141, Apr. 2024.

[9] N. Shlezinger, G. C. Alexandropoulos, M. F. Imani, Y. C. Eldar, and D. R. Smith, "Dynamic metasurface antennas for 6G extreme massive MIMO communications," *IEEE Wireless Commun.*, vol. 28, no. 2, pp. 106–113, Apr. 2021.

[10] R. Deng, B. Di, H. Zhang, D. Niyato, Z. Han, H. V. Poor, and L. Song, "Reconfigurable holographic surfaces for future wireless communications," *IEEE Wireless Commun.*, vol. 28, no. 6, pp. 126–131, Dec. 2021.

[11] D. Dardari and N. Decarli, "Holographic communication using intelligent surfaces," *IEEE Commun. Mag.*, vol. 59, no. 6, pp. 35–41, Jun. 2021.

[12] J. An, C. Yuen, C. Huang, M. Debbah, H. V. Poor, and L. Hanzo, "A tutorial on holographic MIMO communications—Part I: Channel modeling and channel estimation," *IEEE Commun. Lett.*, vol. 27, no. 7, pp. 1664–1668, Jul. 2023.

[13] A. Pizzo, L. Sanguinetti, and T. L. Marzetta, "Fourier plane-wave series expansion for holographic MIMO communications," *IEEE Trans. Wireless Commun.*, vol. 21, no. 9, pp. 6890–6905, Sep. 2022.

[14] J. An, C. Xu, D. W. K. Ng, G. C. Alexandropoulos, C. Huang, C. Yuen, and L. Hanzo, "Stacked intelligent metasurfaces for efficient holographic MIMO communications in 6G," *IEEE J. Sel. Areas Commun.*, vol. 41, no. 8, pp. 2380–2396, Aug. 2023.

[15] J. An, C. Yuen, C. Xu, H. Li, D. W. K. Ng, M. Di Renzo, M. Debbah, and L. Hanzo, "Stacked intelligent metasurface-aided MIMO transceiver design," *IEEE Wireless Commun.*, vol. 31, no. 4, pp. 123–131, Aug. 2024.

[16] J. An, C. Yuen, M. D. Renzo, M. Debbah, H. Vincent Poor, and L. Hanzo, "Flexible intelligent metasurfaces for downlink multiuser MISO communications," *IEEE Trans. Wireless Commun.*, pp. 1–15, 2025.

[17] D. Tse and P. Viswanath, *Fundamentals of Wireless Communication*. Cambridge University Press, 2005.

[18] R. W. Heath, N. González-Prelcic, S. Rangan, W. Roh, and A. M. Sayeed, "An overview of signal processing techniques for millimeter wave MIMO systems," *IEEE J. Sel. Topics Signal Process.*, vol. 10, no. 3, pp. 436–453, Apr. 2016.

[19] O. E. Ayach, S. Rajagopal, S. Abu-Surra, Z. Pi, and R. W. Heath, "Spatially sparse precoding in millimeter wave MIMO systems," *IEEE Trans. Wireless Commun.*, vol. 13, no. 3, pp. 1499–1513, Mar. 2014.

[20] T. S. Rappaport, G. R. MacCartney, M. K. Samimi, and S. Sun, "Wideband millimeter-wave propagation measurements and channel models for future wireless communication system design," *IEEE Trans. Commun.*, vol. 63, no. 9, pp. 3029–3056, Sep. 2015.

[21] A. Hjorungnes and D. Gesbert, "Complex-valued matrix differentiation: Techniques and key results," *IEEE Trans. Signal Process.*, vol. 55, no. 6, pp. 2740–2746, Jun. 2007.